Advances in Materials Research, *Vol. 14, No. 5 (2025) 367-396*
https://doi.org/10.12989/amr.2025.14.5.367

Evaluations of smart self-repaired RC beams

Haysam S. Hassan[1], Ali A. Elkhatib[2], Mohamed M. Ahmed[2] and Adil K. Al-Tamimi*[2]

[1]*College of Engineering, American University of Sharjah, UAE*
[2]*Civil Engineering Department Faculty of Engineering, Assiut University, Egypt*

(*Received June 22, 2023, Revised July 3, 2025, Accepted September 2, 2025*)

Abstract. In this research the author implemented numerous investigations employing finite element analysis (FEA) in order to address the impact of the strengthening techniques with various shear reinforcement ratios on the maximum beam's capacity and their maximum deformations. The previous experimental study by the researchers focused on the development self-restoring mode to monitor the initiated cracks and stress. The performance of RC beams has been enhanced by internally injection ducts, beams strengthened by nitinol smart bars, and beams with a combination of both. They have studied using a three-dimensional (3D) nonlinear finite element (FE) model created by ABAQUS. The FE model incorporates geometric and material nonlinearities in concrete, steel, and Nitinol reinforcement, which is confirmed by comparing beams capacities and failure modes to published literature. The influences of two parameters: (a) strengthening configuration and (b) shear reinforcement ratio are investigated in complete parametric analysis comprising 12 models. Results indicated that The Finite Element model performance is equivalent to the experimental investigation utilized as a reference. The variances in terms of ultimate load capacity did not surpass 5%. when compared to experimental data. The proportion of ACI and FEM ultimate loads varied between 72 and 101 percent. Due to the criteria of safety as prescribed by the ACI to assure conservative design, FEM and the experimental ultimate loads have higher values compared to ACI analytical values.

Keywords: ABAQUS; NiTi Alloy (Nitnol); Nonlinear FEA; Shape Memory Alloy (SMA); Super Elastic effect (SE)

1. Introduction

Because of its ease of use, faster construction, endurance, variety, and cost savings, reinforced concrete (RC) is the most extensively utilized building material in the world. Notwithstanding, these benefits during any occurred earthquake or any sudden impact, reinforced concrete (RC) structure members firstly have elastic behavior up to steel yield limit then the member will be deformed in plastic stage creating some cracks and keeping a residual strain in the reinforcement itself. Steel reinforcement does not have the capability to recover and close the cracks aftermath with converting the plastic joints to elastic joints. Shape Memory Alloy (SMA), a type of intelligent material, has lately been used in the construction of intelligent structures that are exposed to excessive loads. The Super Elastic Effect (SE) kind of Shape Memory Alloy (SMA), which will be widely employed in the construction industry in critical stress zones in the future, is a superior material that can return

*Corresponding author, Professor, E-mail: aliabdzaher0@gmail.com

 ISSN: 2234-0912 (Print), 2234-179X (Online)

to its original shape after deformation caused by loading conditions. The use of NiTi alloy (Nitinol) in reinforced concrete (RC) as hybrid reinforcement with High tensile steel (H.T.S) can enhance the RC member behavior with giving more elasticity to reduce the residual deformation aftermath and cracks breadth. SMAs in concrete elements were only used in a few experimental and modeling studies, and most of them used novel building techniques. This section comprises exploratory studies into the use of SMA as a structural reinforcement which develop nonlinear 3D finite element models and verified against experimental results. The performance of RC beams with intelligent rebars under static transverse loads can be numerically examined using the finite element method, according to Khaloo *et al*. (2010). ANSYS software was utilized to execute a three - dimensional model of the concrete beam; SOLID85 and SOLID185 were utilized to represent the concrete and longitudinal reinforcement, correspondingly. Abdulridha *et al*. (2013) investigated a numerical modeling of RC specimens with SMAs in previous works. As a result, the study stated that superelastic SMAs' has ability to regain inelastic distortion, demonstrate yielding and unit deformation stiffening, and face significant displacement ductility. These are structural properties that grant SMAs an appealing future structure reinforcing option. Malagisi *et al*. (2014) devised a numerical technique for simulating RC beams using SMA actuators in order to fix flexural fissures. The experimental performance of an intelligent RC beam exposed to a three-point bending test was simulated employing finite element simulations. In order to validate the model, the numerical findings were compared to experimental data collected by Daghia *et al*. (2011). The comparison showed that the suggested computational technique is capable of accurately representing the experimental effectiveness of an intelligent RC beam in both the destructive and repairing phases. Finally, this computational technique can be stressed as an effective tool for creating intelligent structural parts. Bin Wang (2018) studies whether SE bars can be used to create self-centering (SC) RC walls. The remaining deformation of SC–RC walls is decreased in this scenario by SE shape memory alloy with substantial regaining the unit deformation and excellent fatigue characteristics. Finite-element program Open Sees was used in this study for modeling and nonlinear analyses (Mazzoni *et al*. 2016). The numerical model for the interplay of axial force, bending moment, and shear force is depicted. Halahla *et al*. (2019) investigated the impact of exchanging traditional steel reinforcement in concrete with SMA on the analysis of RC joints subjected to varied applied loads and the results showed the displacement capacity of RC beam rose significantly as well as the ductility capabilities raised. The damage-plasticity modeling and finite element analysis employing the ABAQUS program were similarly successful in properly anticipating cracking commencement, yielding, and mode of failure according to the author. This allows this strategy to be applied to more complex issues in a wider variety of conditions and locations. Ruiz-Pinilla *et al*. (2020) reported a finite element model (FEM) according to an experimental investigation that looked into the use of iron-based shape memory alloy (Fe-SMA) strips for exterior shear strengthening of small-scale RC specimen. The author concluded that the stress-strain formulae and numerical simulation model created might be used in additional research to assess the efficiency of Fe-SMA strips of different settings outwardly reinforcing RC beams in shear. Ji *et al*. (2022) depicted an experimental and analytical study to analyze the shear behavior of the RC beam constructed with (Fe-SMA) stirrups and observed that the failure mechanism of the RC beam actively confined through Fe-SMA was exactly predicted using Finite Element analysis model. The author reported that the utmost load of the elements anticipated by the analysis varied by less than 5% from the experiment data. As a result, the studied finite element analysis model can accurately estimate the shear performance of RC members fabricated by Fe-SMA stirrups.

In RC beams, which are the emphasis of this Finite Element Analyses research, adding only

Nitinol rods to H.T.S reinforcement or adding internal injected ducts as well as using both of them as strengthening strategies for these RC beams with various shear reinforcement ratios were experimentally studied by the Authors Hassan *et al*. (2022).They concluded that the improvement in the utmost load by 12% contrasted to the reference specimens. Khalil *et al*. (2022) stated that FEA software was used to computationally analyze the structural behavior of RC beams enhanced with Fe-SMA rebars (ABAQUS). A parametric analysis was done to determine the effects of various concrete grades, pre-stressing intensities, and the size of Fe-SMA bars on the load-deflection behavior once the FEM has been verified. Furthermore, the chosen strengthening method utilizing Fe-SMA bars is contrasted with alternative methods frequently employed in the building industry. The authors came to the conclusion that raising the concrete grade from 30 to 60 MPa results in an increase in the cracking, steel yielding, and ultimate loads for the test specimens of 15%, 4%, and 0.75 percent, correspondingly. According to Yeong-Mo *et al*. (2022), the FE simulation model was created to study the bending responses of RC beams, taking into account nonlinear material characteristics including concrete crushing and cracking in addition to plastic deformation of the Fe-SMA bars. In accordance with the authors' summary, the projected bending load from the FE simulations was 20–30 kN greater than the actual experiment results. This was believed to be caused by the FE simulations' usage of Fe-SMA rods and concrete under the highly idealized perfect bonding assumption. The elasticity of the reinforced concrete beam with NiTi rods increases gradually and depends on the type of loading, according to research by Bykiv *et al*. (2022) using finite element modeling (FEM) to study the strengthening of the reinforced concrete beam by shape memory alloy at the place of maximum loading and deflection under 3- and 4-point bending. In contrast to conventional reinforcing, residual deflection decreased under 3-point bending by 24% and under 4-point bending by 27%. In the beam containing nitinol rods, however, maximum stresses are 6% greater in the first cycle and 5% larger in the second cycle, whereas residual stresses are 2.3% less in the first cycle and 4.3% less in the second cycle.

The Research gaps as mentioned above in previous studies have gradually in last two decades concentrated on using the SMA bar as RC structure reinforcement, hybrid with steel reinforcement, strengthening beam-column joint, strengthening the column-foundation joint, improving the structure restoring system and pre-stressed alloy in side RC Structure. The present study gives more accurate results than previous studies when the author used the combination between the intelligent rod and internal injection method compared with experimental study. In the previous studies, the authors used only the intelligent bars without internal injection method added in the present study to use the advantage of both in recovering and repairing the occurred cracks. Future research are required to gain more information and analyses about the restoring methods which will be useful to reduce the risk and damages for structures with maintaining sustainability during seismic circumstances and aftermath.

1.1 Research objective

The numerical results for a reinforced concrete beam subjected to flexural loading in various strengthening techniques with only internally injected method, adding Nitinol intelligent bars or with both of them are compared to experimental data in this work. The method is to protect and reduce the damages in the building concrete structure after sudden movement due to earthquakes or explosions by retaining the members in elastic behavior to their original shape by SMA-SE and in the same time to fill the occurred cracks by automated injection method linked with building failure control management system which will give instruction to proceed the injection such as fire alarm

Table 1 Tested beams details

Series	Beam ID	Ast (mm) H.T.S stirrup	Self -repair inwardly injected ducts	An (mm) Nitinol intelligent rods	*fcu (MPa)*
I	A1	Ø8 @300 mm	0	0	65
	B1	Ø8 @300 mm	2 ducts	0	70
	C1	Ø8 @300 mm	0	2Ø 4	65
	D1	Ø8 @300 mm	2 ducts	2Ø 4	70
II	A2	Ø8 @150 mm	0	0	65
	B2	Ø8 @150 mm	2 ducts	0	70
	C2	Ø8 @150 mm	0	2Ø 4	65
	D2	Ø8 @150 mm	2 ducts	2Ø 4	70
III	A3	Ø8 @100 mm	0	0	65
	B3	Ø8 @100 mm	2 ducts	0	70
	C3	Ø8 @100 mm	0	2Ø 4	65
	D3	Ø8 @100 mm	2 ducts	2Ø 4	70

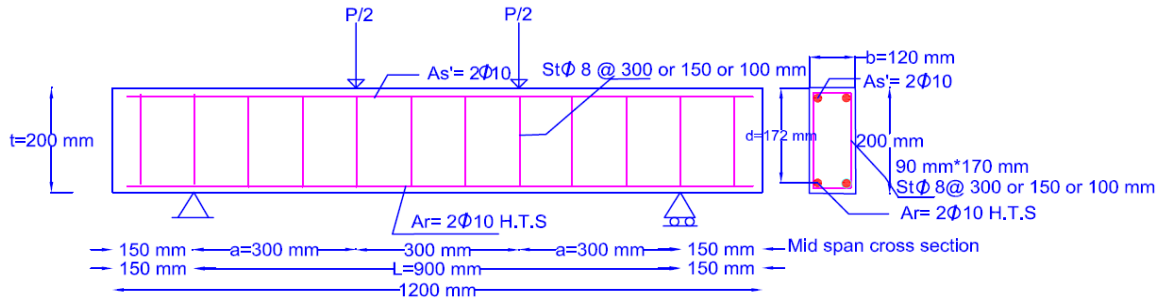

Fig. 1 Specimens A1, A2, A3 details

system. The finite element model (FEM) results focused on obtaining the load-displacement charts, combined stress and plastic strains for the entire tested beams. The beams capacities values from FEM were contrasted to the experimental and analytical findings.

All Beams have width (b)=120 mm, thickness (t) = 200 mm, Span length (L) = 900 mm, a/d=1.7, bottom H.T.S reinforcement 2Ø10 and top H.T.S reinforcement.

2. Materials and methods

The FEA conducted the RC beams in the experimentally published study by the authors Hassan, Haysam *et al*. 2022. Twelve RC beams were experimentally tested; these beams consisted of 3 series I, II, III, where each has four kinds of specimens as presented in Figs. 1-3 and Table 1.

Specimens (D1, D2, and D3) were similar to kind (A), but they had two inner curved ducts (holes) 10 mm dia. utilized for inner epoxy injection as indicated in Fig. 2, as well as two Nitnol rods with a 4 mm dia. curvature design with the same precision in Fig. 3.

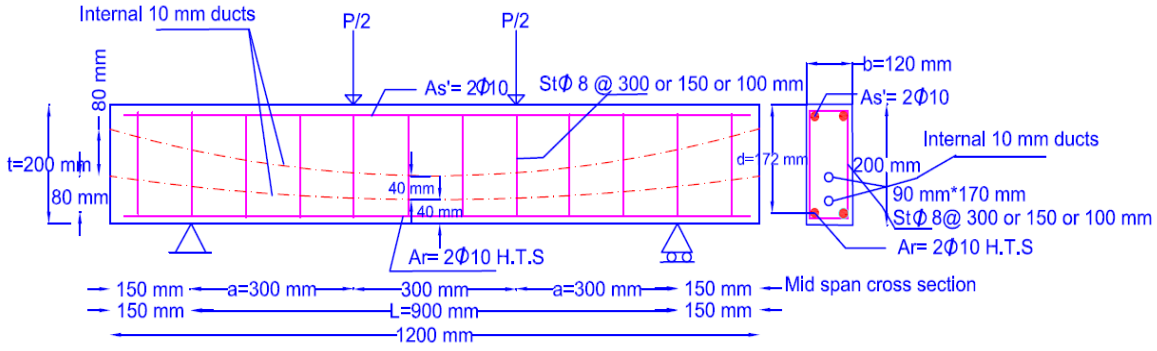

Fig. 2 Specimens B1, B2, B3 details

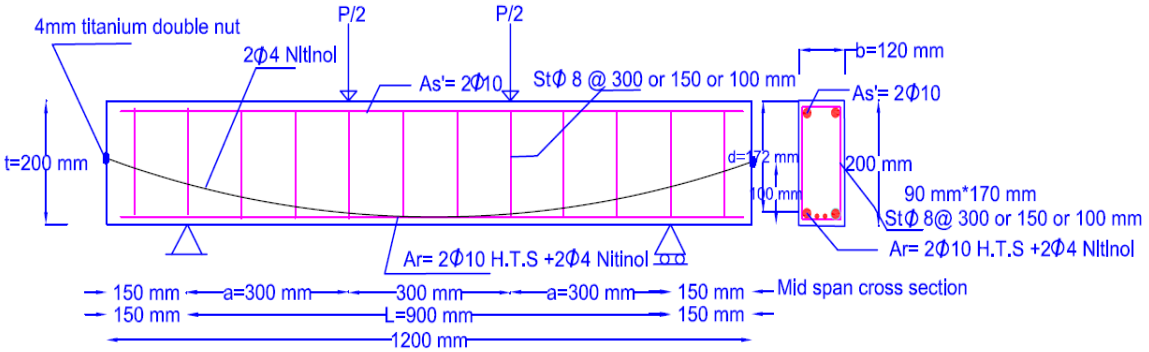

Fig. 3 Specimens C1, C2, C3 details

2.1 Concrete

Compressive behavior of concrete is linear until tiny cracking occurs, at which point it becomes nonlinear until utmost compressive strength is reached, causing a reduction in strength as strain increases. Under uniaxial tension, concrete behaves in a linear elastic manner up to failure stress (equivalent to the commencement of micro cracking). The softening is followed by a brittle failure path. Fig. 4 depicts the compressive and tensile stress–strain relationships for the concrete strengths of 65 MPa and 70 MPa employed in this investigation. To characterize concrete behavior, a variety of methodologies with differing levels of expertise might be applied. The capability of a constitutive model for concrete behavior to describe mechanical characteristics such as softening, fissure formation/propagation, and concrete damages are chosen. For modeling concrete structures, ABAQUS offers three constitutive models: namely cracking model for concrete (CMC), concrete smeared cracking model (CSCM) and concrete damaged plasticity model (CDPM). The discrete Concrete crack model (CMC), wherein cracks are established at element boundaries, and the compressive concrete reaction was simulated using Drucker Prager perfect plasticity, is a common approach. CMC designed for applications in which the behavior is dominated by tensile cracking and assumes that the compressive behavior is always linear elastic. CMC must be used with the linear elastic material model (“Linear elastic behavior,” Section 17.2.1), Pawtucket (2014), which also defines the material behavior completely prior to cracking.

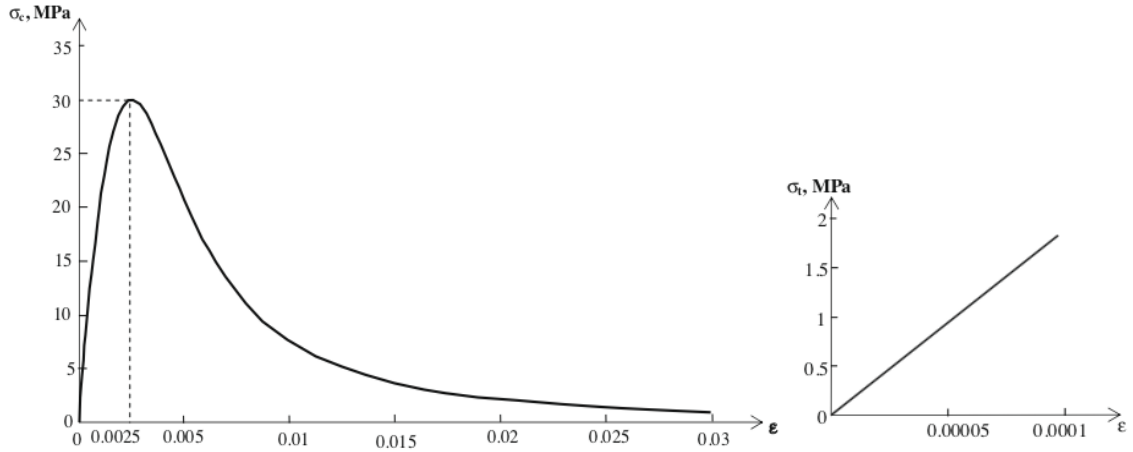

Fig. 4 Concrete compression and tension behavior

Table 2 Properties Test Report of the used steel 10 mm and 8mm bars (3 samples for each).

Parameters	Test report						BS 4449-2005	compliance
	10 mm			8 mm				
Elongation at maximum force, Ag(%)	8.5	8	8.5	7	6.5	8	5.0 % Min.	comply
Yield strength, Re (N/mm²) or MPa	555	561	556	537	511	531	500 Min.	comply
Tensile strength, Rm (N/mm²) or MPa	641	644	640	608	602	614	N/A	comply
Stress Ratio (%)	1.15	1.15	1.15	1.13	1.18	1.16	1.08 Min.	comply
Deviation from nominal cross section	-2.9	-2.9	-3.4	-3.8	-4.1	-3.8	±4.5	comply

Table 3 CDP Behavioral Model Parameters.

CDP Parameters				
Dilation Angle	Eccentricity	Fbo/Fco	K	Viscosity Parameter
36	0.1	1.16	0.667	0.0001

The Concrete smeared crack model (CSCM) is built on the concept of concrete cracks whenever the principal tensile stress crosses the tensile strength of the material. In the direction parallel to the principal tensile stress direction, the material's elastic modulus is assumed to be negligible. CSCM uses oriented damaged elasticity concepts (smeared cracking) to describe the reversible part of the material's response after cracking failure. CSCM requires that the linear elastic material model (see "Linear elastic behavior," Section 21.2.1) be used to define elastic properties; and cannot be used with local orientations (see "Orientations," Section 2.2.5) Pawtucket (2014).

The concrete damage plasticity model (CDPM) technique has been shown to be useful in anticipating the results of ordinary concrete tests in tension and compression, and it assigns nonlinear material behavior to two separate material mechanical procedures: plasticity and damage mechanisms. The CDP model from ABAQUS software product was used to simulate the inelastic behavior of concrete in this research. The plastic damage model requires the input of elastic modulus, Poisson's ratio, plastic damage parameters and a description of compressive and tensile behaviour from constitutive models. The dilation angle is the angle of internal friction of concrete material and

oscillates between 30° to 40°, the flow potential eccentricity is a small positive number that defines the rate at which the hyperbolic flow potential approaches its asymptote, fb0/fc0 parameter represents the ratio between the concrete compressive strength in biaxial state and the concrete compressive strength in uniaxial state, k is the ratio of the second stress invariant on the tensile meridian to that on the compressive meridian, and the viscosity parameter defines visco-plastic regularization. Poisson's ratio is defined as 0.2. The five plastic damage parameters recommended by the Abaqus manual Pawtucket (2014), for defining concrete material are presented in Table 3.

Concrete compressive and tensile behavior for 65 MPa and 70 MPa compressive strengths was defined using a modified constitutive model of the original Popovic's model coupled with literature-based plastic damage models Obaidat (2011). This model defined compressive cracking and tensile softening as the two basic concrete failure mechanisms. Eq. (1) is used to calculate the concrete modulus of elasticity:

$$E_c = 4700\sqrt{f'_c} \tag{1}$$

where E_c is the concrete elastic modulus and f'_c is the concrete compressive strength in MPa.

Eq. (2) is used to calculate the stress-strain response. Khalil *et al*. (2022):

$$\sigma_c = \frac{E_c \varepsilon_c}{1 + (R + R_E - 2)\left(\frac{\varepsilon_c}{\varepsilon_0}\right) - (2R - 1)\left(\frac{\varepsilon_c}{\varepsilon_0}\right)^2 + R\left(\frac{\varepsilon_c}{\varepsilon_0}\right)^3} \tag{2}$$

where: $R = \frac{R_E(R_\sigma - 1)}{(R_E - 1)^2} - \frac{1}{R_E}$, $R_E = \frac{E_c}{E_0}$, $E_0 = \frac{f'_c}{\varepsilon_0}$, $\varepsilon_0 = 0.003$ $(ultimate\ compressive\ strain)$, $R_\sigma = 4$, $\nu = 0.2$ $(poisson's\ ratio)$

Eq. (3) can be used to derive inelastic strain (ε_{in}) from total strain:

$$\varepsilon_{in} = \varepsilon_c - \varepsilon_0 \tag{3}$$

The concrete reaction under uniaxial tension is believed to be linear elastic up to the failure stress reached. The pre-peak tensile response was calculated using the equation below.:

$$f'_{ct} = 0.33\sqrt{f'_c} \tag{4}$$

where f'_{ct} is the tensile strength and f'_c is compressive strength in MPa.

The fracture energy approach, specified as the area under the softening curve (assumed to be 90 J/m2) Obaidat (2011), was used to determine the post-peak tensile failure performance of the concrete.

2.2 Reinforcements

Up to the yield stress, when nonlinear behavior starts until the ultimate tensile stress is reached, steel behaves in an initial linearly elastic zone proportionate to the elastic modulus. Complete fracture occurs at maximum strain, and the necking of the steel begins after ultimate point. Fig. 5 illustrates a typical stress-strain response for reinforcing steel and Fig. 6 shows an idealized steel stress-strain curve Kyaure and Farid (2021).

As seen in Fig. 6, ductile reinforcing steel is typically believed to have an elastic-plastic constitutive relationship for ordinary engineering applications used for simulation models, with or without strain hardening. Steel is supposed to exhibit some hardening following yielding in an elastic hardening model, according to Supaviriyakit *et al*. (2004). According to Neale *et al*. (2005),

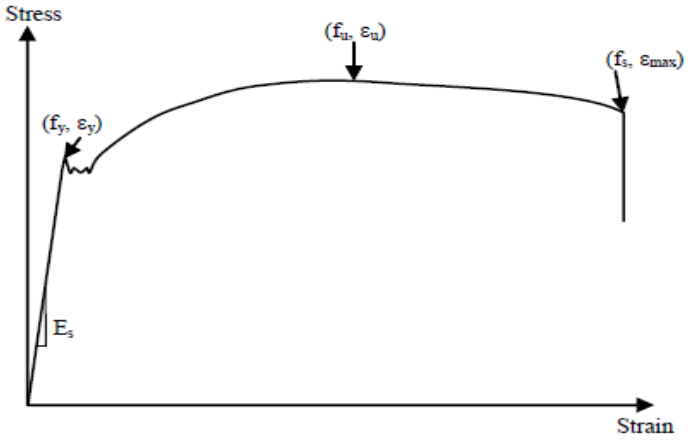

Fig. 5 Tensile stress-strain curve for typical reinforcing steel bar (Kyaure and Farid 2021)

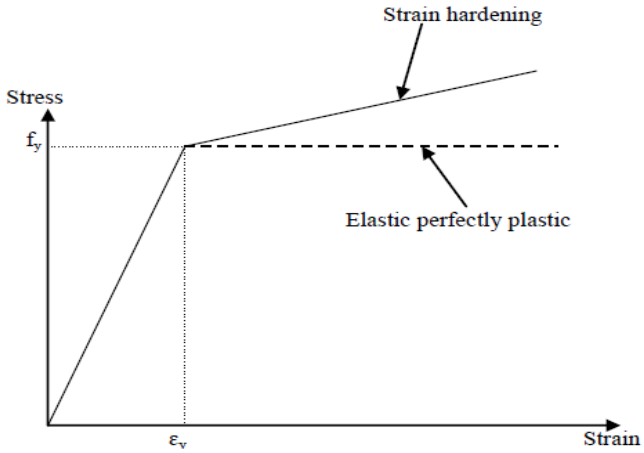

Fig. 6 An idealized steel stress-strain curve (Kyaure and Farid 2021)

An elastic-perfectly-plastic model typically produces findings that are satisfactory for RC members' reaction prediction. The H.T.S and Nitinol reinforcement are treated as an elastic completely plastic material that behaves the same in tension and compression in this investigation. A yield strength of 500 MPa, an elastic modulus of 200 GPa, and a Poisson's ratio of 0.3 were used to simulate longitudinal and transverse steel reinforcements. The tensile strength of Nitinol intelligent reinforcement is 1000 MPa with 0.26 elongation. The material at point (A) undergoes a change when it is stressed at a constant temperature when in a stable austenite phase, as shown by the curves in Fig. 7. The material undergoes an elastic deformation from point (A) to point (B), when the martensitic transformation starts. The strain increases until it reaches its maximum level at point (C), causing the transition between points (B) and (C) to occur under constant stress. Notably, the SMA material and its intended use determine the highest strain level that can be achieved. The behavior is defined by a new curve, as shown in the stress-strain curve Fig. 7, and is known as the stress "plateau," which is the curved area that joins points (B) and (C). Reaching point (C) signifies that the austenite to martensite phase transition is complete.

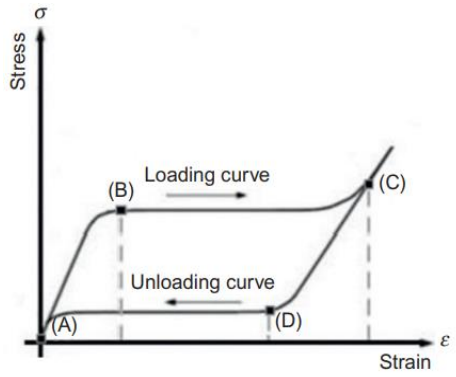

Fig. 7 SMA-SE (Nitinol) stress-strain

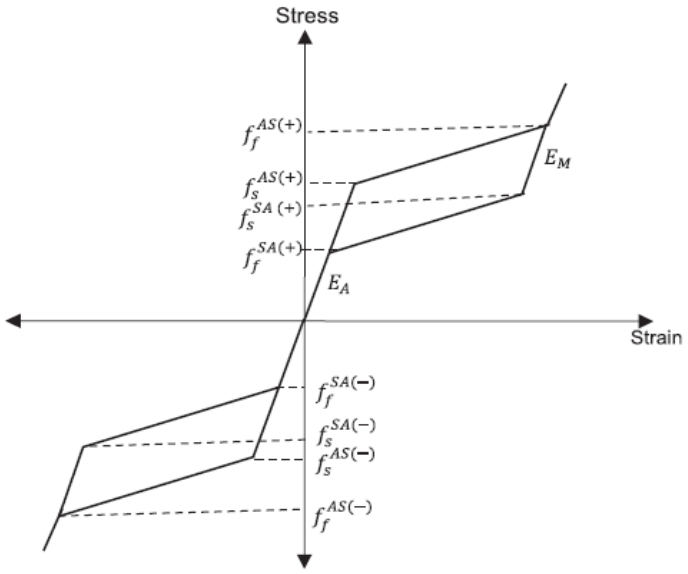

Fig. 8 SMA Model Presented by Auricchio and Sacco (1997), Mohammadgholipour (2023)

Auricchio and Sacco (1997), Mohammadgholipour (2023), used Euler Bernoulli beam theory to create a one-dimensional superelastic SMA model. In Figure 8, the suggested constitutive model is displayed. This model explains how the material behaves under tension and compression, as well as how austenite and martensite differ in their elastic characteristics. Both the conventional flag-shaped response and full strain recovery are considered in this model.

Through the use of multiple numerical examples, the behavior of a beam cross section under pure bending was examined. SMA's distinct forward and reverse transformation stress behavior leads to the conclusion that it exhibits distinct moment curvature relationships in tension and compression.

The research of Auricchio and Sacco (1997), and Auricchio and Taylor (1997), Mohammadgholipour (2023). served as the foundation for the super elasticity model included in ABAQUS. The single-variant martensite reorientation process for SMAs, superplastic behavior, and distinct material behavior in tension and compression were all replicated by the suggested model. The models utilized in ABAQUS is displayed in Fig. 9.

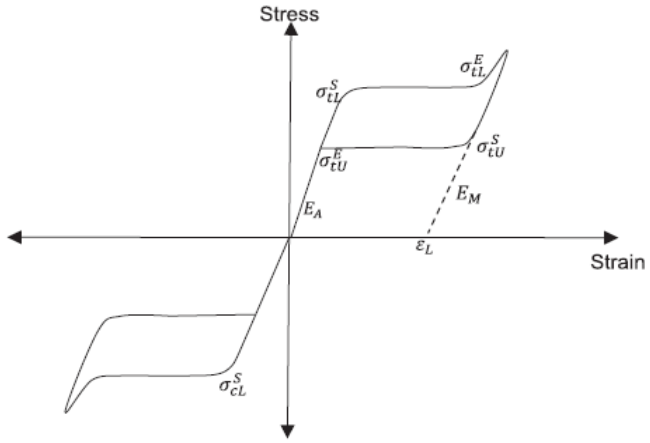

Fig. 9 Constitutive models used in ABAQUS Mohammadgholipour (2023)

The temperature effect, loading frequency and the asymmetric behavior of SMAs were considered In Abaqus but the effect of buckling is not considered. In ABAQUS, (Austenite-to-martensite starting stress parameter) should be defined to consider the asymmetric behavior of SMAs.

2.3 Internal injection epoxy

In simulation models, the internally injected epoxy material (Master inject 1315 from BASF supplier) was not considered as separate material such concrete and the reinforcement (H.T.S &Nitinol). The effect of the internal injection just increased the concrete compressive strength from 65 MPa to 70 MPa as average test result from rebound hammer tests for concrete beams after injection by 48 hrs in the experimental study by the authors Hassan *et al*. (2022).

3. Finite element modeling by ABQUS program

3.1 Model geometry

With reduced integration, an eight-node linear 3D solid element (C3D8R) was employed to simulate concrete. Beam reinforcement, both conventional steel and intelligent bar, was modelled using two-node linear 3D truss elements (T3D2). Figs. 10-12 show model geometries for concrete and steel elements.

3.2 Boundary conditions & constraints

Using the embedded region constraint, a perfect bond is assumed to simulate the interaction among concrete and reinforcement. Four rigid plates are modeled in contact with the beam to represent a four-point loading which includes two loading plates on the top face of the beam and two support plates on the bottom face of the beam. On the rigid plates' reference points, a

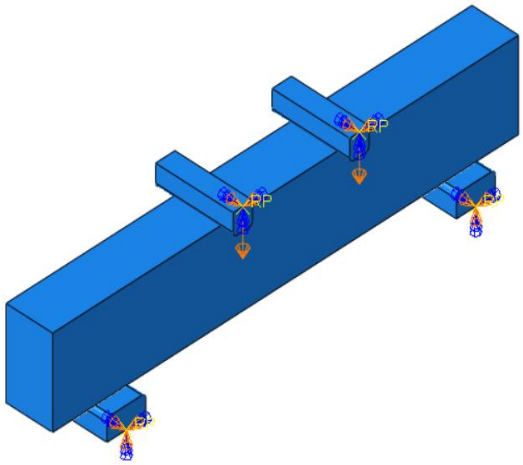

Fig. 10 Model geometry for concrete beams

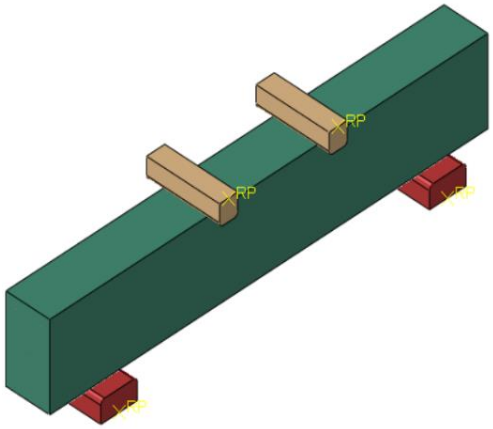

Fig. 11 Model Geometry shows the supporting and loading points

displacement-controlled boundary condition is assigned. Modelling parameters and element kinds are derived from the literature Kyaure *et al*. (2032).

3.3 Loading condition

A linearly rising displacement ranged from 0.1 to 0.0001 mm step increment is used to model the static loading condition. The infinitesimal increment allows for a continuous step displacement regulated investigation to estimate the peak and post peak load characteristics of the beam. The rigid plates were located at the loading points to distribute the load to avoid the top beam crushing in the early stage of loading due to the impact of the concentrated loads. The entire specimens were subjected to a four-point static bending test included or excluded internal injection technique in one or two phases as previously done in the experimental study Hassan *et al*. (2022). Two phases imply loading from zero to 80% of the utmost force, then offloading to 0% of the utmost load, monitoring

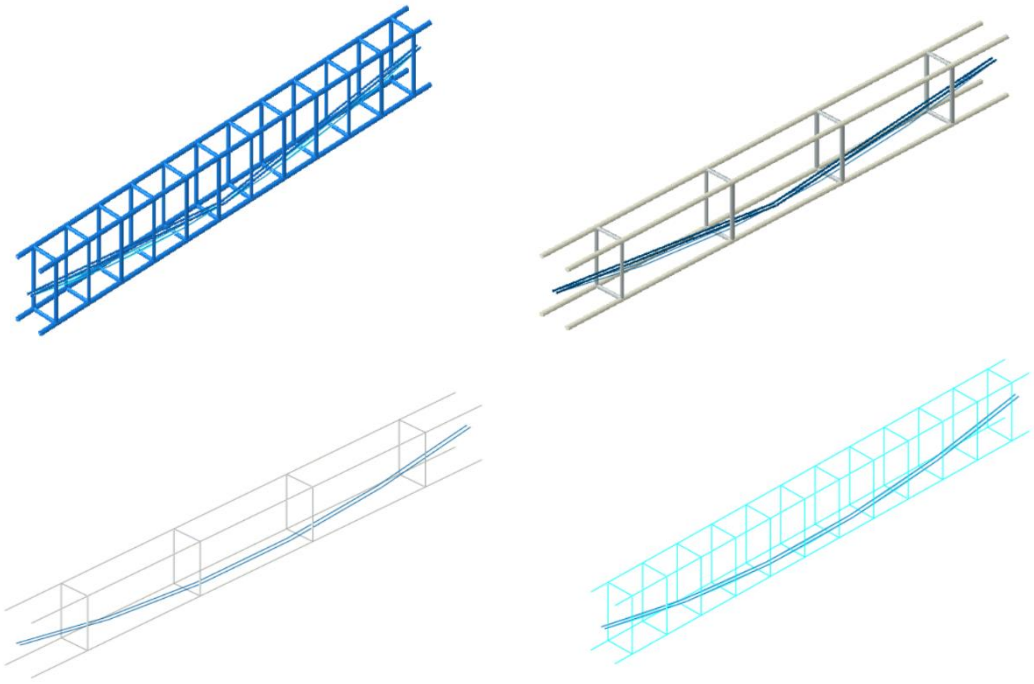

Fig. 12 Model Geometry for steel and Nitinol reinforcement in the beams

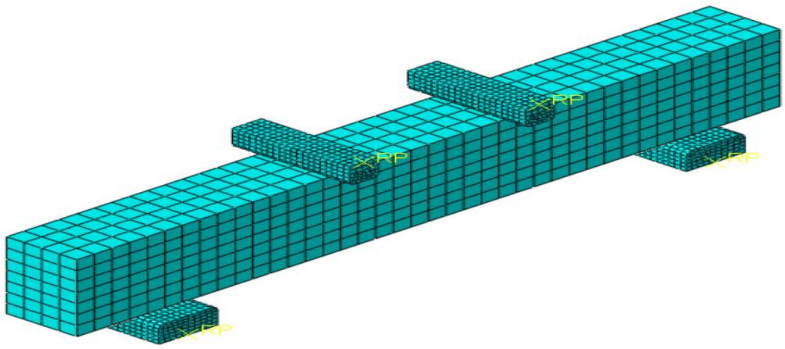

Fig. 13 Mesh sensitivity analysis in the beams

the crack width, and finally reloading to 80% of the utmost load. When the injection occurred by an electrical low-pressure injection pump, the loading was maintained constantly. The same load was applied for another 48 hours, after which the beams with internal injection ducts were loaded until they failed. Nonetheless, unlike the previous situations, beams with only intelligent bars might continue loading in the second phase till failure without any interruption. For the beams having internal injections, the concrete compressive strength has improved from 65 MPa to 70 MPa.

Since the ABAQUS modeling can only deal with one concrete compressive strength CPD properties in each phase without change during running the model, the loading cases were separately conducted in each phase before and after the injection with different concrete CPD inputs.

3.4 Mesh configuration & sensitivity analysis

Mesh sensitivity analysis is performed on 3D models to determine the suitable mesh size and to quickly replicate the experimental findings. In all models, a mesh size of 25 mm is chosen after using different sizes as the optimal size for concrete RC beams based on mesh sensitivity analysis, as illustrated in Fig. 13. Orthotropic behavior usually defines RC beams. Since this mesh is interwoven bi-directionally, isotropy is assumed. Quadratic order meshing was more accurate than linear order meshing. Free meshing is the most flexible meshing technique since it uses no pre-established mesh patterns and can be applied to almost any model shape such as Tetrahedral elements or hexahedral elements.

3.5 Convergence problems

Many methods were used to assure convergence, including employing tiny time increments, diminishing mesh size when using the high-strength concrete, and using intelligent Nitinol bars in two static phase loadings in RC beams to maintain analytical continuity.

3.6 Model verification

A comparative with the findings of a study conducted by the authors Hassan *et al*. (2022) confirmed the suggested FE analysis methodology. 12 RC beams were examined experimentally; these specimens consisted of three series: I, II, and III, that each had 4 varieties of specimens as illustrated in Figs. 1, 2, and 3. The suggested FE analysis model was verified using the material model described in Section 2, and the numerical values for each material's properties were taken from sources Hassan *et al*. (2022).

3.7 Result outcome

The results of the finite analysis modeling were in excellent accord with those of the experiments. The utmost loads, load- displacement charts, steel stress, concrete combined stress (S, Mises), Stress in bending direction (S33), deflection (U, Magnitude) and Plastic strain (PE, P33) values were obtained from the outcomes data given by ABAQUS finite element analyses program.

The first loading phase was identical to the second phase in the same graph line up to 80% of utmost force for the corresponding control beams for the specimens having inner injected ducts, having only Nitinol rods and beams having both of them as shown in the Load- displacements chart due to occurring in the elastic stage prior to steel or Nitinol yielding.

ABAQUS program did not consider the small, injected ducts as a void due to their less cross section area compared with beams cross section. The ducts cross section area 0.65% of the full beam cross section and according to an AS Elamary (2021) study, utilizing lower than 10% of the beam cross-section as the hollow part had no significant impact on the utmost load and beam capacity.

4. Parametric study

Finite Element models are improved to analyze the behavior of concrete beams reinforced by The High Tensile Steel (H.T.S) used as stirrups, bottom and top bars in the examined RC beams in the laboratory while inner channels and/or SE Nitinol rods were added to the beams, which were

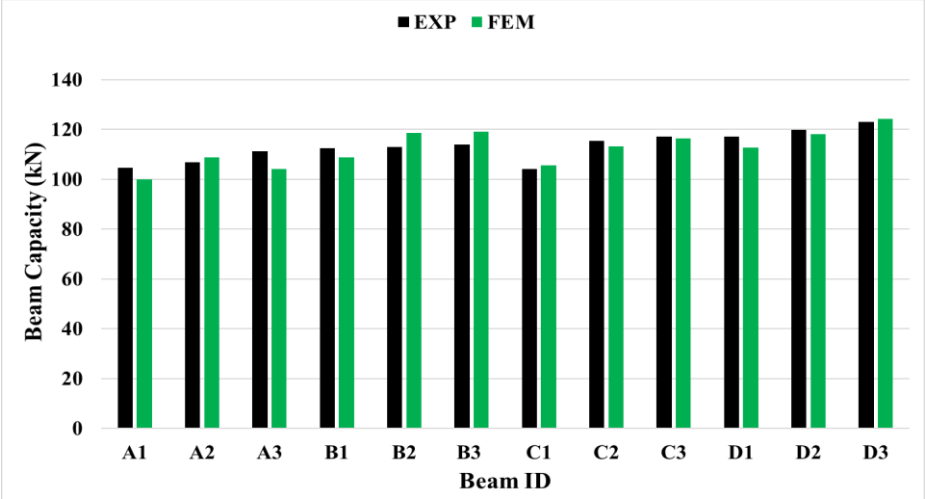

Fig. 14 Finite element modeling and experimental values for ultimate load

Table 4 Finite element modeling and experimental values for ultimate load

Beam Types	Specimen ID	FEM	EXP	% DIFF	RATIO FEM/EXP
A	A1	100	105	5	0.96
	A2	109	107	2	1.02
	A3	104	111	7	0.94
B	B1	109	112	3	0.97
	B2	119	113	5	1.05
	B3	119	114	4	1.04
C	C1	106	104	1	1.01
	C2	113	115	2	0.98
	C3	116	117	1	0.99
D	D1	113	117	4	0.96
	D2	118	120	1	0.99
	D3	124	123	1	1.01

then examined against static stress through 2 phases (loading – un loading) until fail. The following parameters are taken into account in the research:

1. Sort of bottom reinforcement rods (Nitinol and /or H.T.S).
2. Shear reinforcement ratios ($\rho_w = A_{sw} / (s \cdot b_w \cdot \sin\alpha)$) where Asw = Total area of stirrups legs crossing the crack/spacing (mm2) &S= stirrup spacing & bw=beam width.
3. Specimens including or excluding channels inwardly injected by master inject 1315 (low viscosity epoxy substance manufactured by BASF)

The parameters listed above were selected to investigate their influence on the total behavior of reinforced specimens, mostly on the cracks shape, mode of failure, vertical displacement, unit deformation, flexural, and shear strength. 12 numbers RC specimens were manufactured and

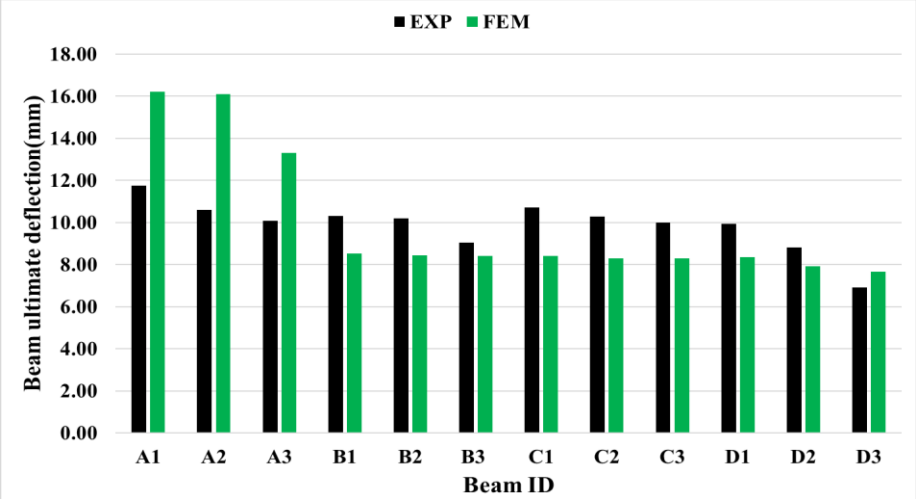

Fig. 15 Finite element modeling and experimental values for ultimate deflections

Table 5 FEM and Experimental Values for Maximum Deflection at Ultimate Load

Beam Types	Specimen ID	FEM	EXP	% DIFF	RATIO FEM/EXP
A	A1	16.20	11.76	27	1.38
	A2	16.10	10.59	34	1.52
	A3	13.30	10.08	24	1.32
B	B1	8.51	10.32	21	0.82
	B2	8.45	10.20	21	0.83
	B3	8.40	9.03	7	0.93
C	C1	8.40	10.71	28	0.78
	C2	8.29	10.29	24	0.81
	C3	8.30	9.98	20	0.83
D	D1	8.35	9.94	19	0.84
	D2	7.92	8.80	11	0.90
	D3	7.67	6.92	10	1.11
			AVG	20.5	1.005

separated into three series I, II, and III, with four categories of beam specimens A, B, C, and D in each series, as illustrated in Figs. 1,2,3 and Table (1).

5. Results analysis and discussions

5.1 Finite element modeling ultimate loads

Fig. 14 and Table 4 show the FEM ultimate load compared to the corresponding experimental values in the entire investigated beams. The ratio between FEM and experimental ultimate loads

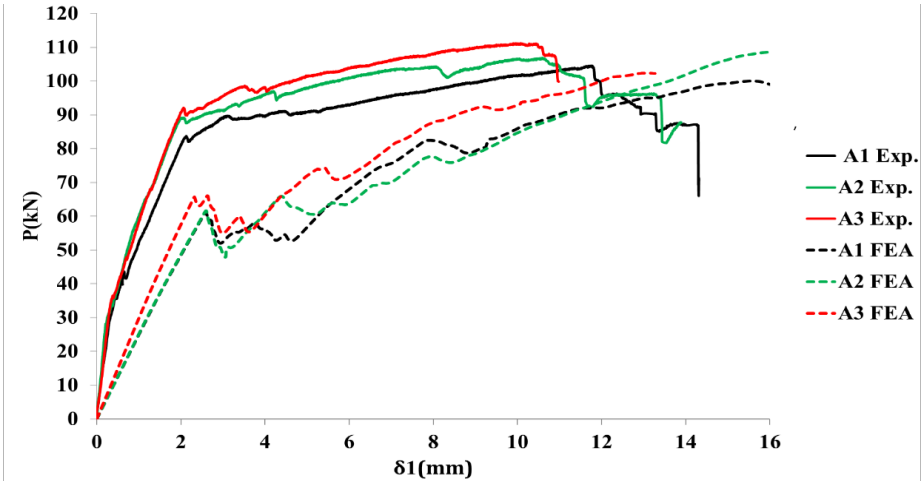

Fig. 16 Finite element modeling and experimental load-displacement chart in beams type A

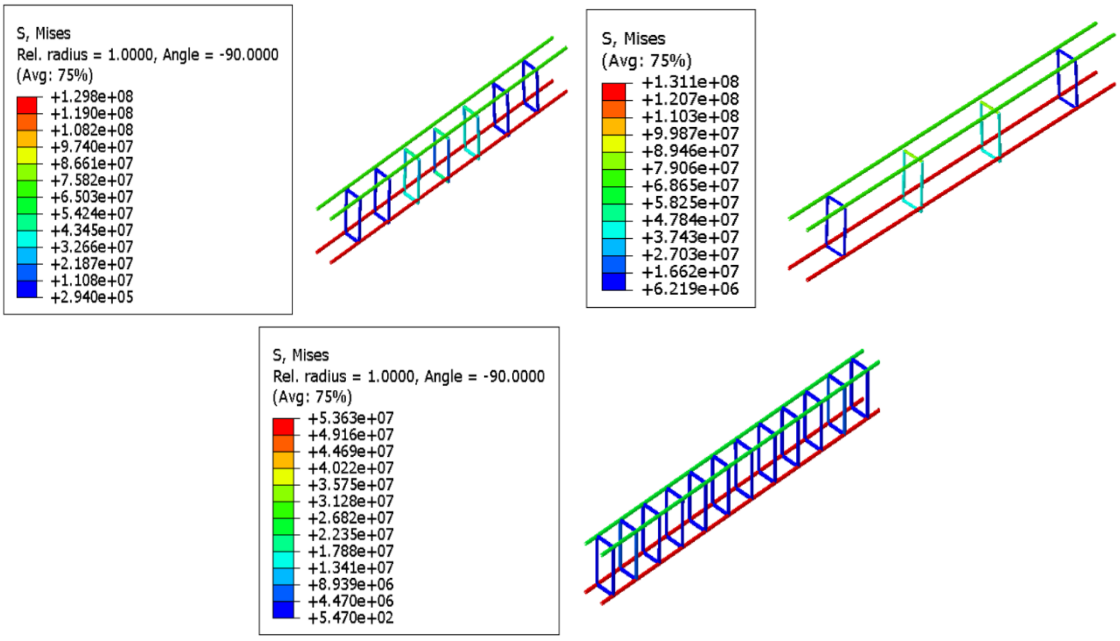

Fig. 17 Stress Contour in Reinforcement Beams A1, A2, A3

ranged from 96% up to 105%. The less difference between FEM and experimental ultimate loads can guide the structure engineers to use the modeling in wide range instead of executing more experimental works in the lab.

5.2 Finite element modeling deflection at ultimate loads

Fig. 15 and Table 5 show the FEM ultimate deflections compared to the corresponding experimental values in short and long tested beams. In the short beams (A, B, C, D), the ratio between

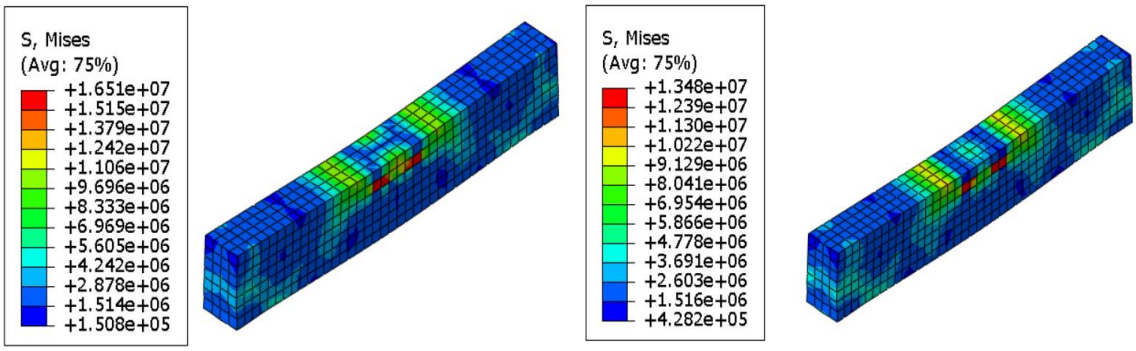

Fig.18 Sample Stress Contour in Concrete Beam Type A

FEM and experimental ultimate deflections ranged from 78% up to 138%.

5.3 Beams Type (A, B, C, D) Results

5.3.1 Beams Type (A)

Fig. 16 showed the Finite Element Modeling and Experimental load-displacement chart in beams type A control beams. It was clearly seen that the beams FEM deflection values were higher than the corresponding experimental beams at any load level and it was diminished with increasing the shear reinforcing ratio. Fig. 17 depicted the Stress Contour in Reinforcement Beams A1, A2, A3. It was noticeable that the maximum stress was at the main bottom bars and it was increased with increasing the beam capacity. For instance, the max. FEM steel reinforcement tensile stress result for Beam A3 equaled to 5.36 e+7 N/m² less the max. experimental steel reinforcement tensile stress which was 5.8 e+8 N/m² due the conservative in the combined stress results in ABAQUS program. Fig. 18 presented the Stress Contour in Concrete Beam Type A. It was clearly noticed that the high stress area was between and underneath the loading points and the center portion at bottom of the beam. Stress increased gradually by increasing the applied load with transferring less stress away from those two areas having the max. stress. For instance, the max. FEM concrete compression stress result for Beam A3 equaled to 1.65 e+7 N/m² near to the max. experimental concrete compression stress which was 2 e+7 N/m². Fig. 19 showed the deflection and plastic strain contour in Concrete Beam A3. It was noted that the high deflection was at the mid span as presented in the experimental study and the highest plastic strain values for all beams type A have indicated similar to cracks patterns which occurred in the experimental beams. The max. FEM concrete plastic strain result at the top Beam A3 equal to 0.00086 near to the max. experimental concrete plastic strain which was 0.00096 while the max. deflection for beam A3 equaled 13 mm near to the max. experimental deflection which was 11 mm. The first crack for the beam (A3) began from the bottom side of pure moment zone at mid span at vertical load equals to 28 kN. When the applied load increased gradually the formed cracks propagated upward and several new cracks were initiated in the tension zone. These cracks started from the bottom of concrete surface and propagated up to comp. zone. Under higher loading crack began to appear in the shear zone from the bottom side nearest to the loading points and propagate in the inclined direction towards the loading point. This indicates that the experimental and Finite Element Modelling studies to define the cracking pattern locations and mode of failure are in great accord.

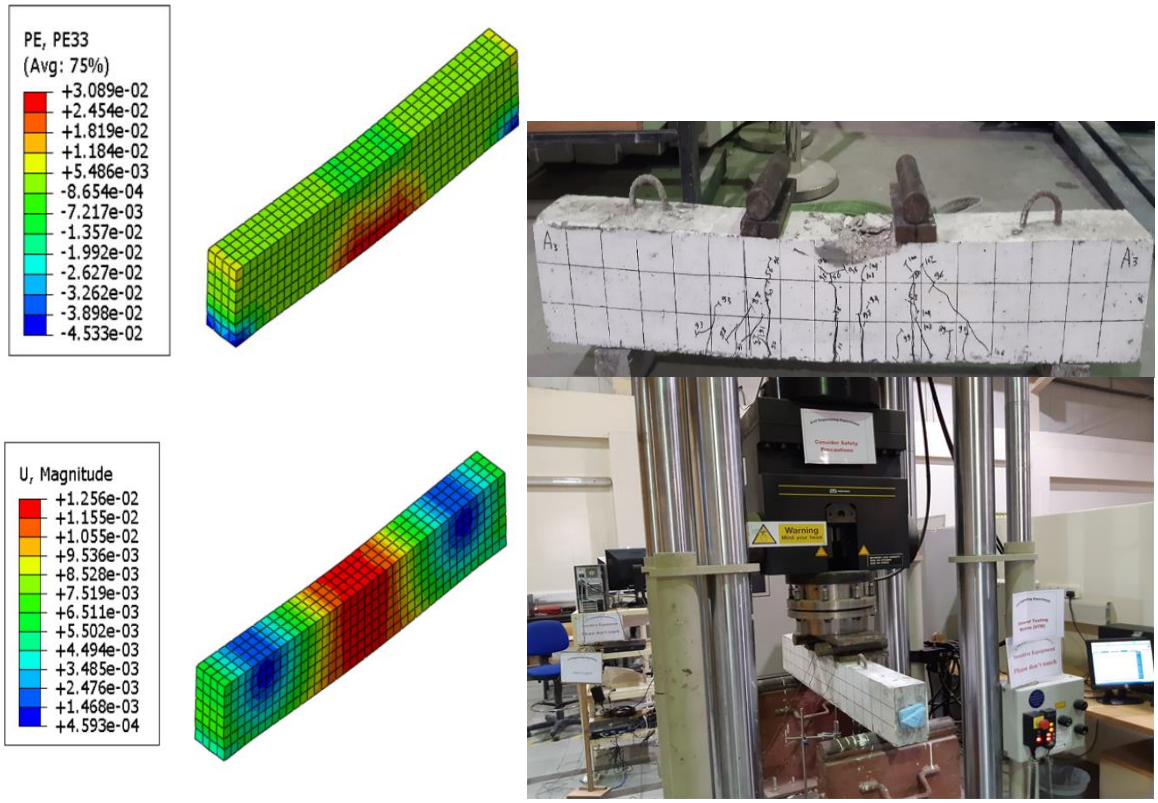

Fig. 19 Deflection and plastic strain in Concrete Beam A3

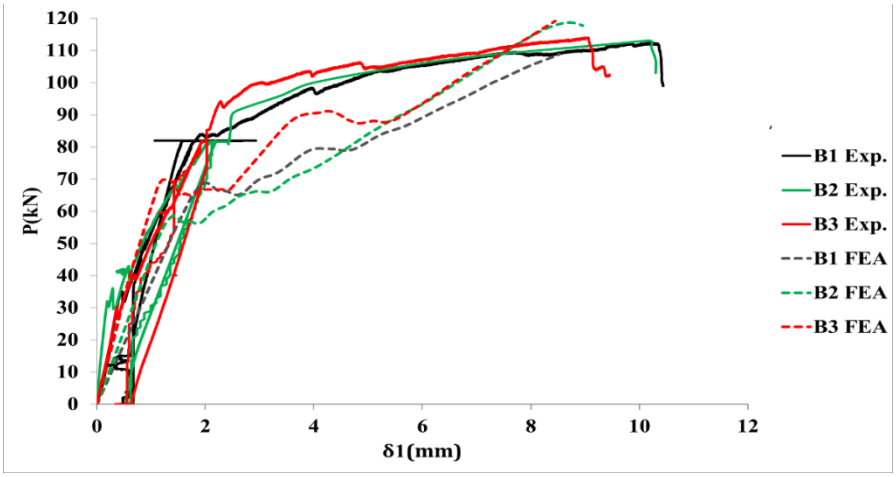

Fig. 20 Finite element modeling and experimental load-displacement chart in beams type B

5.3.2 Beams Type (B)

Fig. 20 showed the Finite Element Modeling and Experimental load-displacement chart in beams type B (Beams having only internal injected ducts). It was clearly given that the beams FEM

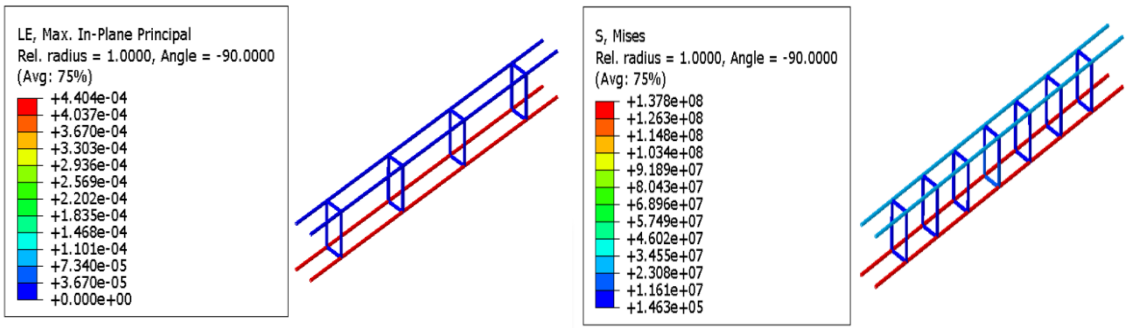

Fig. 21 Stress Contour in Reinforcement Beams B1, B2

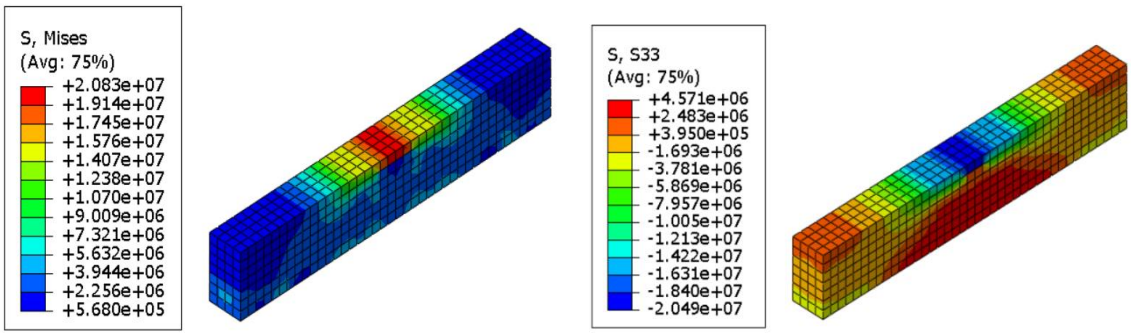

Fig. 22 Stress Contour in Concrete Beam B3

deflection values were higher than the corresponding experimental beams at any load level up to 80 % of the ultimate loads and it decreased with increasing the shear reinforcing ratio. Fig. 21 depicted the samples of Stress Contour in Reinforcement Beams Type B. It was noticeably seen that the maximum combined stress was the main bottom bars, and it increased with increasing the beam capacity. For instance, the max. FEM steel reinforcement tensile stress result for Beam B2 equaled to 1.4 e+8 N/m² less the max. experimental steel reinforcement tensile stress which was 5.7 e+8 N/m² due the conservative in the combined stress results in ABAQUS program Fig. 22 presented the Stress Contour in Concrete Beam Type B. It was clearly mentioned that the high stress area was between and underneath the loading points and the center portion at bottom of the beam. Stress increased gradually by increasing the applied load by transferring less stress away from those two areas having the max. stress. For instance, the max. FEM concrete compression stress result for Beam B3 equaled to 2.08 e+7 N/m² near to the max. experimental concrete compression stress which was 2.1 e+7 N/m². Fig. 23 showed the combined deflection and plastic strain contour in Concrete Beam B3. It was noted that the high deflection was at the mid span as presented in the experimental study and the highest plastic strain values for all beams type B indicated like cracks patterns which had occurred in the experimental beams with less width and number compared to beams type A. The max. FEM concrete plastic strain result at the top Beam B3 equaled to 0.00075 near to the max. experimental concrete plastic strain which was 0.00096 While the max. FEM deflection for beam B3 equals 8.5 mm near to the max. experimental deflection which was 9 mm. The first crack for beam (B3) began from the bottom side of pure moment zone at mid span at vertical load equaled to 30 kN. Increasing the applied load gradually up to 80 kN, in two loading

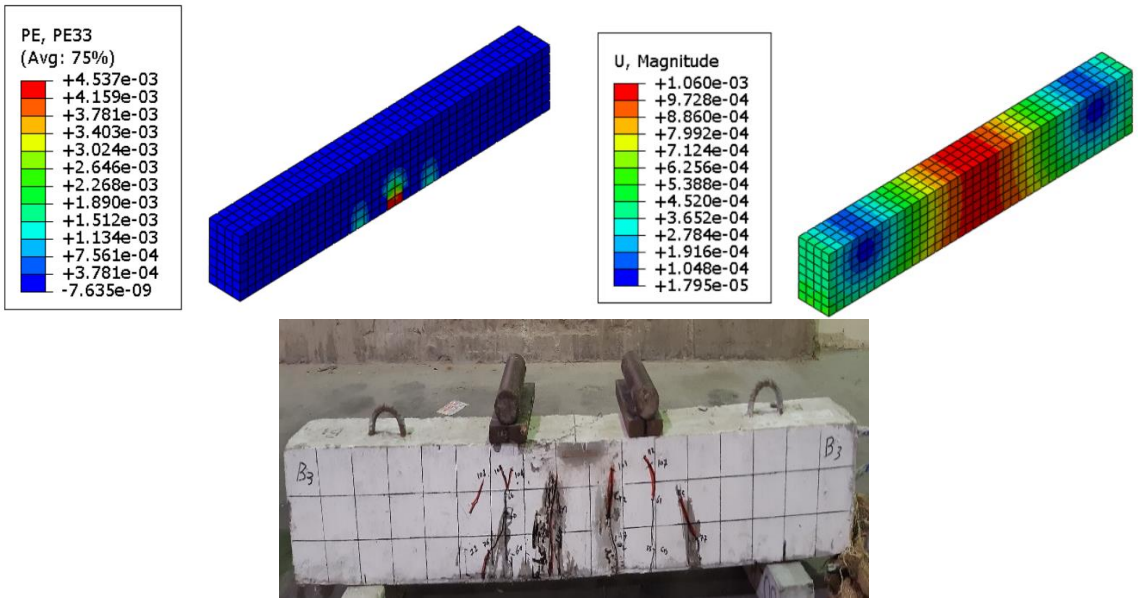

Fig. 23 Deflection and plastic strain in Concrete Beam B3

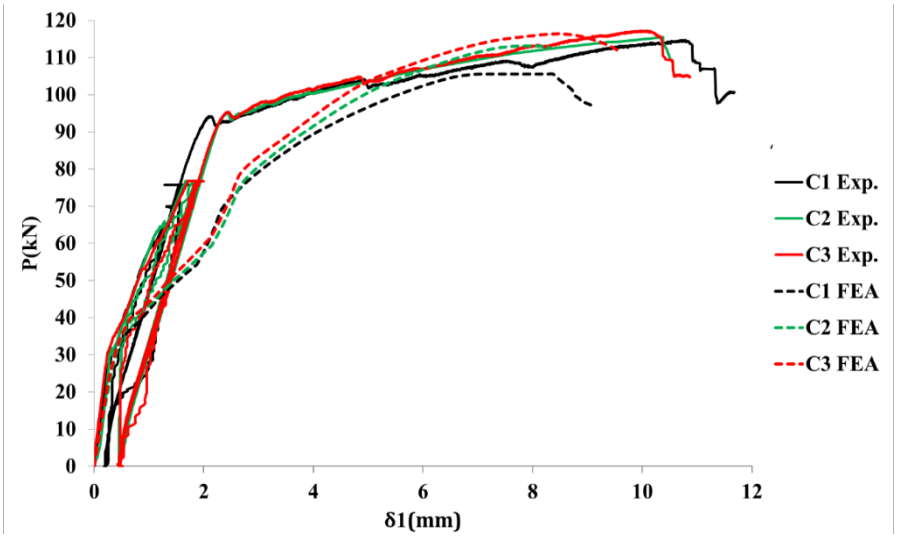

Fig. 24 Finite Element Modeling and Experimental load-displacement chart in beams type C

cycles, the first crack widened, propagated and three new flexural cracks were observed in the tension zone, these started also from the bottom of concrete surface and propagated up to 2/3 of the beam depth toward the comp. zone. When the loading had increased up to 80 kN, two inclined shear cracks were propagated toward loading points. After the releasing load up to zero load, the cracks were partially closed with smaller width in an elastic behavior in the first cycle. In the second cycle, after the loading had been increased up to 80 kN, this load was kept constant while the injection was carried out by electrical low pressure injection pump. The same load was kept further for 48

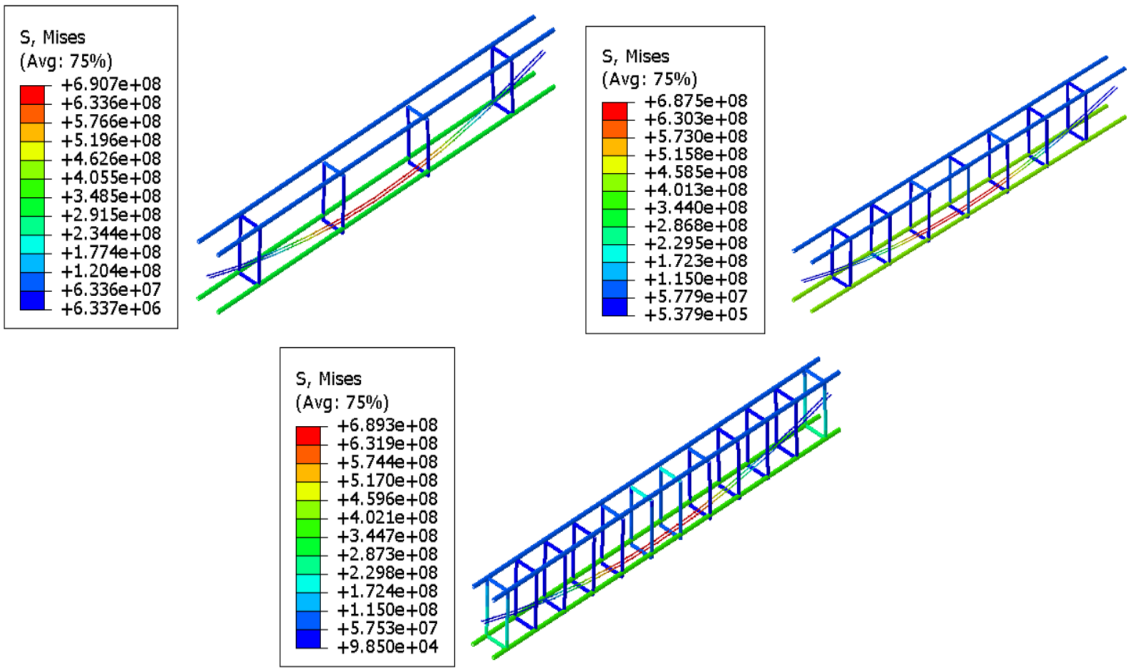

Fig. 25 Stress Contour in Reinforcement Beams C1, C2, C3

hours then continued loading up to failure. This indicates that the experimental and Finite Element Modelling studies to define the cracking pattern locations and mode of failure are in great agreement.

5.3.3 Beam Type (C)

Fig. 24 showed the Finite Element Modeling and Experimental load-displacement chart in beams type C (Beams having only Nitnol intelligent rods). It was clearly presented that the beams FEM deflection values were higher than the corresponding experimental beams at any load level up to 80 % of the ultimate loads and it was lowered with increasing the shear reinforcing ratio. Fig. 25 depicted the samples of Stress Contour in Reinforcement Beams Type C. It was noticeably given that the maximum combined stress was the Nitinol bars at the mid of span zone and it increased with increasing the beam capacity. For instance, the max. FEM steel reinforcement tensile stress result for Beam C3 equaled to 4 e+8 N/m² less the max. experimental steel reinforcement tensile stress which was 5.8 e+8 N/m² due the conservative in the combined stress results in ABAQUS program while the max. FEM Nitinol reinforcement tensile stress result for Beam C3 equaled to 6.8 e+8 N/m² in accord with the max. experimental Nitinol reinforcement tensile stress which was 6.3 e+8 N/m² Fig. 26 presented the Stress Contour in Concrete Beam Type C. It was clearly depicted that the high stress area was between and underneath the loading points and the center portion at bottom of the beam. Stress increased gradually by increasing the applied load by transferring less stress away from those two areas having the max. stress. For instance, the max. FEM concrete compression stress result for Beam C3 equaled to 3.01 e+7 N/m² near to the max. experimental concrete compression stress which was 2.98 e+7 N/m². Fig. 27 showed the combined deflection and plastic strain contour in Concrete Beam C3. It was noted that the high deflection was at mid span as

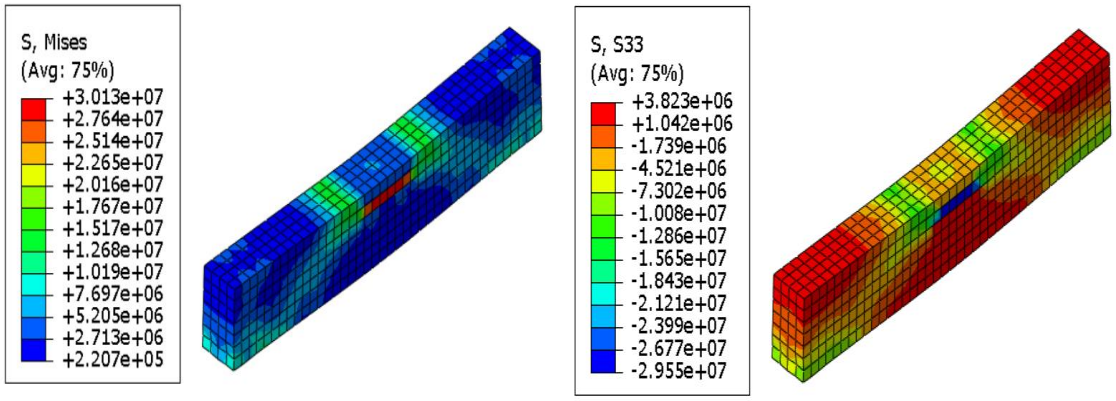

Fig. 26 Stress Contour in Concrete Beam C3

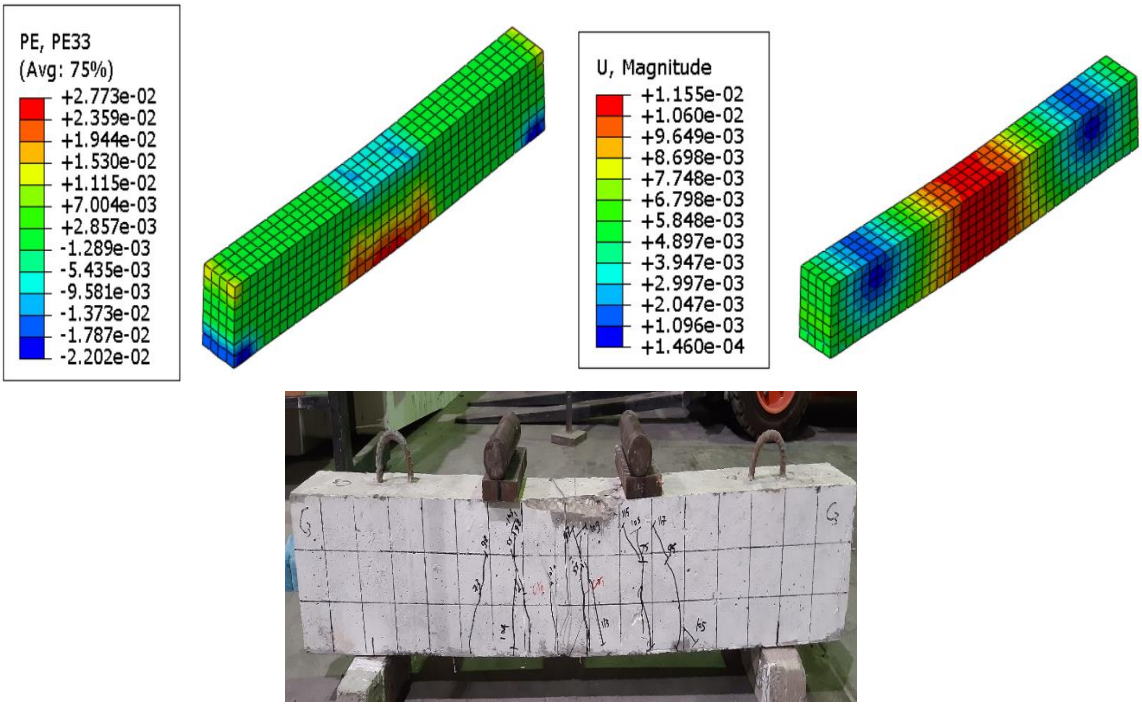

Fig. 27 Deflection and plastic strain in Concrete Beam C3

mentioned in the experimental study and the highest plastic strain values for all beams type C was indicated to be like cracks patterns occurred in the experimental beams with less width and number compared to beams type A and B. The max. FEM concrete plastic strain result at the top Beam C3 equaled to 0.00128 near to the max. experimental concrete plastic strain which was 0.00105 while the max. FEM deflection for beam C3 equal to 8.4 mm near to the max. experimental deflection which was 10 mm. The initiation of the first crack for beam (C3) began from the bottom side of pure moment zone at mid span at vertical load equals 32 kN. Increasing the applied load gradually

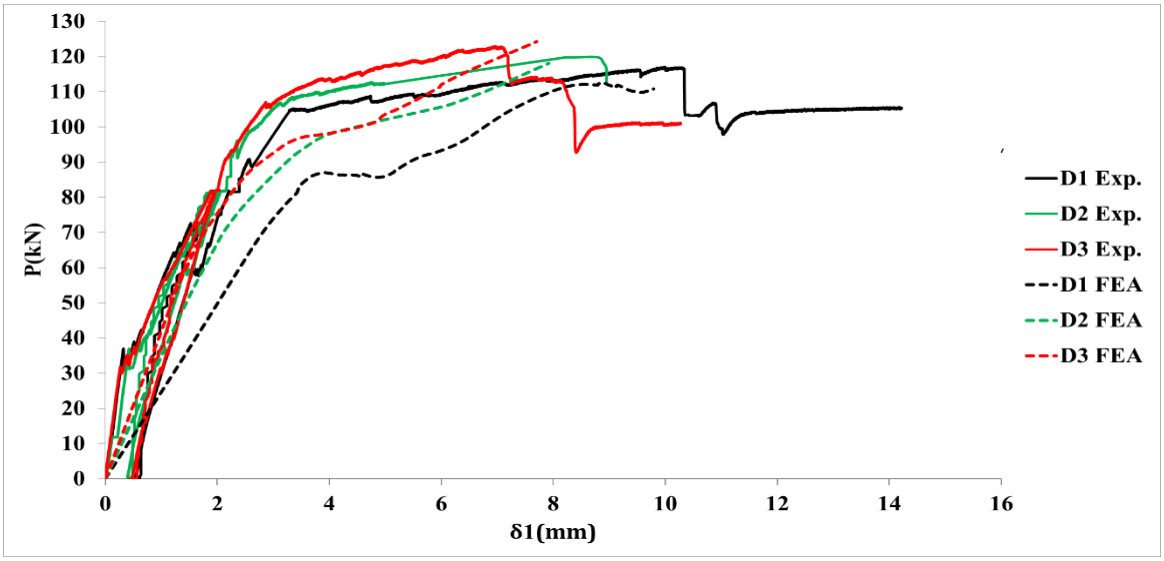

Fig. 28 Finite Element Modeling and Experimental load-displacement chart in beams type D

up to 75 kN in two loading cycles, the first crack widened, propagated and new flexural cracks were observed in the tension zone. These started also from the bottom of concrete surface and propagated up to 2/3 of the beam depth toward the comp. zone. When the loading was increased up to 75 kN then released up to zero load, the cracks fully closed due to the elastic behavior of the embedded smart bars. After investigating all cracks in these two cycles up to 75 kN was done, the loading continues from 75kN up to the failure. This indicates that the experimental and Finite Element Modelling studies to define the cracking pattern locations and mode of failure were in great harmony.

Fig. 28 showed the Finite Element Modeling and Experimental load-displacement chart in beams type D (Beams having both Nitinol intelligent rods and internal injected ducts). It was clearly depicted that the beams FEM deflection values were higher than the corresponding experimental beams at any load level and it was diminished with increasing the shear reinforcing ratio. Fig. (29) showed the samples of Stress Contour in Reinforcement Beams Type D. It was noticeably given that the maximum combined stress was the Nitinol bars at the mid of span zone and it increased with increasing the beam capacity. For instance, the max. FEM steel reinforcement tensile stress result for Beam D2 equaled to 4.1 e+8 N/m² less the max. experimental steel reinforcement tensile stress which was 5.4 e+8 N/m² due the conservative in the combined stress results in ABAQUS program while the max. FEM Nitinol reinforcement tensile stress result for Beam D2 equaled to 6.8 e+8 N/m² in accord with the max. experimental Nitinol reinforcement tensile stress which was 6.3 e+8 N/m². Fig. (30) presented the Stress Contour in Concrete Beam Type D. It was clearly depicted that the high stress area was between and underneath the loading points and the center portion at bottom of the beam. Stress increased gradually by increasing the applied load by transferring less stress away from those two areas having the max. stress. For instance, the max. FEM concrete compression stress result for Beam D3 equal to 3.5 e+7 N/m² near to the max. experimental concrete compression stress which was 3 e+7 N/m². Fig. (31) showed plastic strain contour in Concrete Beams D1&D3. It was noticed that the highest plastic strain values for all beams type D indicated to be like cracks patterns noted in the experimental beams with less width

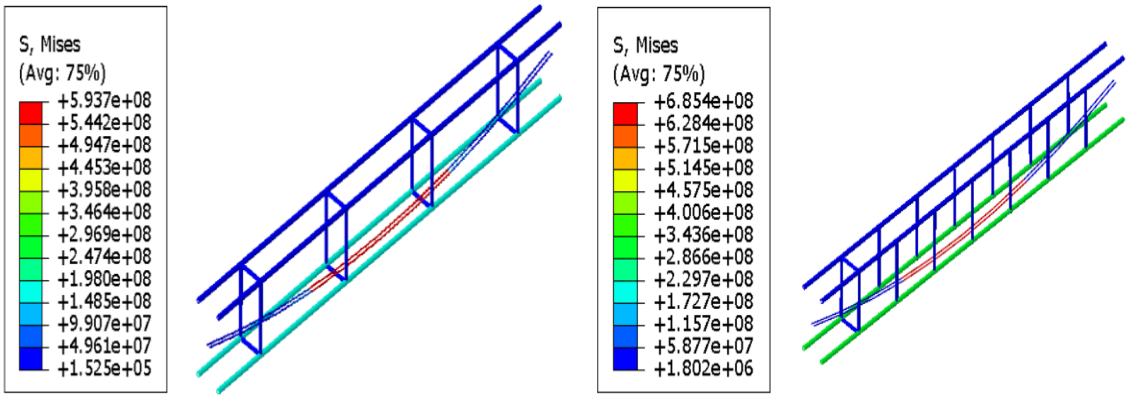

Fig. 29 Stress Contour in Reinforcement Beams D1, D2

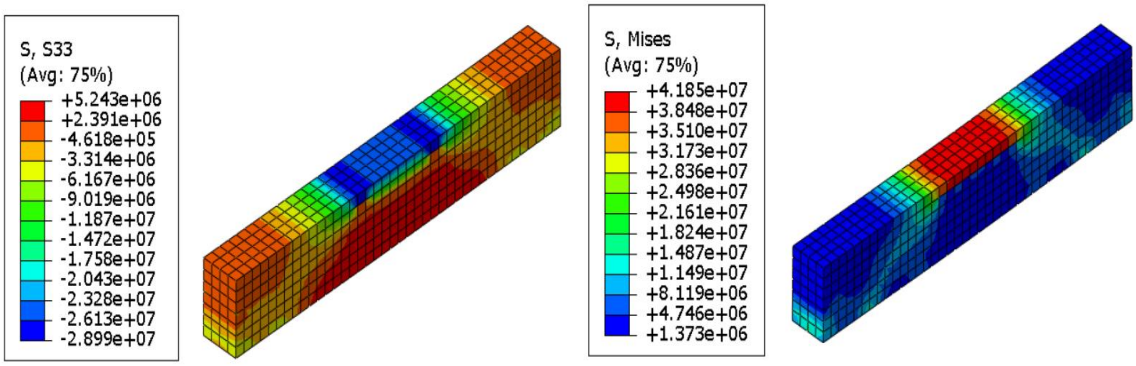

Fig. 30 Stress Contour in Concrete Beam D3

and number compared to beams A, B and C. The max. FEM concrete plastic strain result at the top Beam D3 equaled to 0.0006 near to the max. experimental concrete plastic strain which was 0.00075 while the max. FEM deflection for beam D3 equal to 7.5 mm near to the max. experimental deflection which was 7 mm. The first crack for beam (D3) began from the bottom side of pure moment zone at mid span at vertical load equaled to 35 kN. Increasing the applied load gradually up to 80 kN in two loading cycles, the first crack widened, propagated and six new flexural cracks were observed in the tension zone, half of these cracks started also from the bottom of concrete surface and propagated up to 1/3 of the beam depth and the balance cracks propagated up to 2/3 of the beam depth toward the comp. zone. When the loading increased up to 80 kN then released up to zero load, the cracks fully closed with smaller width due to the elastic behavior of the embedded smart bars in the first cycle. In the second cycle, after the loading had been increased up to 80 kN, this load was kept constant while the injection was carried out by electrical low pressure injection pump. The same load was kept further for 48 hours then continued loading up to failure. This indicates that the experimental and Finite Element Modelling studies to define the cracking pattern locations and mode of failure are in great accord.

Figs. 16, 20, 24, 28 illustrate the comparison of experimental data and ABAQUS results for the load deflection curves for the investigated beams. Because the post-failure phase of ABAQUS is

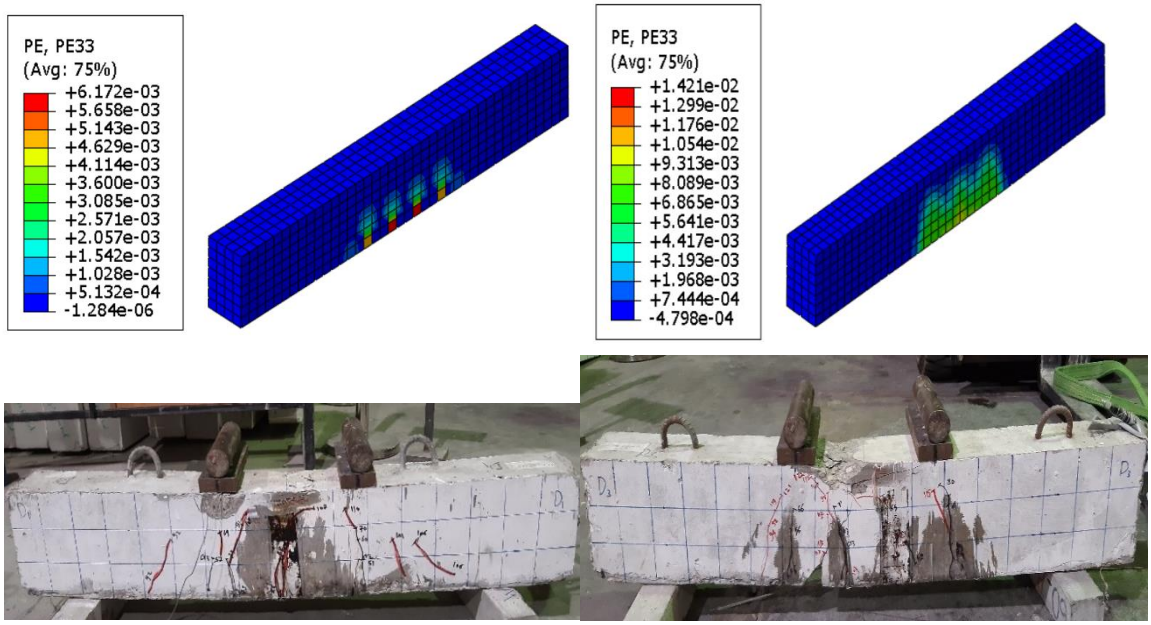

Fig. 31 plastic strain in Concrete Beams D1, D3

not adequately represented, the curves are shown up to the failure point. There is a significant disparity between the values obtained from experiments and those estimated using finite element analysis when comes to the ultimate deflection values. One reason for this could be because the post-cracking rigidity and modeling of reinforced concrete elements are not effectively represented, which is another area that needs to be further investigated. In general, the load–deflection curves predicted using ABAQUS followed the same pattern as those acquired by experiment. The ultimate load results are summarized in Table 4. For all tested beams, the variances in terms of ultimate load capacity did not surpass 5%. When compared to experimental data, the conclusions derived from the finite element analysis in terms of the ultimate load showed a reasonable consistency.

In addition, there are also differences between the analysis and experimental test deflection findings, which might be due to various factors:

1. Despite the fact that finite element models presume homogeneous, symmetric, and similar contact forms among cells, the constitution of real concrete, which comprises cement, sand, gravel, and other components, is highly complex. The intricate motion between them cannot be easily replaced by a unified form.

2. The bonding among concrete and steel is addressed using Integrated Innovation in Finite Element Analysis, successfully simplifying the modeling; however, with higher load of reinforced concrete and mutability of the resistance moment, particularly reinforced slip simulation, this is not practicable. This can simply cause inaccurate results.

3. The analysis is influenced by the accuracy of the Finite Element Analysis, the appropriateness of simulation parameter magnitudes, the form and quantity of finite element segment, pouring quality, and the loading circumstances of the beam in the test.

In short, the finite element method for nonlinear beam test analysis has a significant level of correlation with the existing scenario: notwithstanding minor inconsistencies, the finite element analysis for nonlinear beam test analysis is feasible.

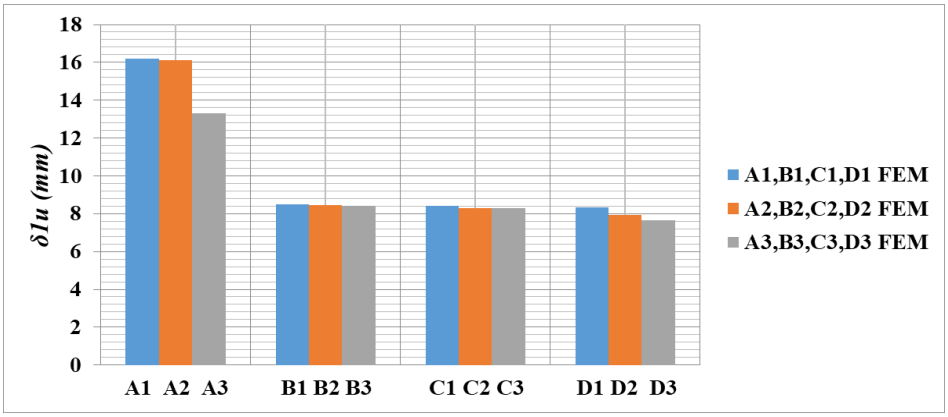

Fig. 32 The FEM deflection versus strengthening techniques

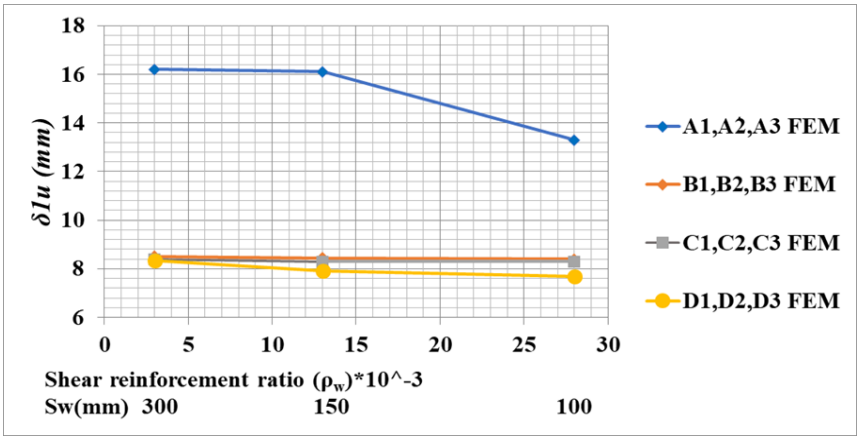

Fig. 33 The deflection versus shear reinforcement ratio (ρw)

5.4 Strengthening techniques effect on FEM vertical displacement at utmost loads

Fig. 32 presents the FEM mid-span vertical displacement at utmost load (δ1u) for the entire specimens with various strengthening strategies. The FEM vertical displacement at utmost load (δ1u) was diminished using several strengthening approaches in control specimens, specimens with inwardly injected ducts, specimens with intelligent rods, and specimens having both of them correspondingly. Outcome data presented reduction in vertical displacement magnitudes in series III, II, I specimen correspondingly as the shear reinforcement ratio raised, and the obtained magnitudes for the entire tested specimens are given in Table 5.

Specimens shear reinforcement ratio (ρ_w) versus FEM vertical displacement at utmost load for the entire specimens are depicted in Fig. 33. It was observed that the magnitudes diminished with rising specimen shear reinforcement ratio (ρ_w). The less magnitudes were in kinds (D), (C), (B) and (A) specimens correspondingly.

FEM vertical displacement at utmost load (δ1u) for specimens (B1), (C1), and (D1) was 53 percent, 52 percent, and 51 percent correspondingly, when contrasted to the collaborated magnitude for specimen (A1), and 52 percent, 51 percent, and 49 percent for specimens (B2), (C2), and (D2)

Table 6 ACI Equation, FEM and experimental Ultimate loads Values

Beam Type	Specimen ID	ACI	FEM	EXP	% DIFF	RATIO FEM/EXP	RATIO ACI/FEM
A	A1	72	100	105	5	0.96	0.72
	A2	95	109	107	2	1.02	0.87
	A3	95	104	111	7	0.94	0.91
B	B1	78	109	112	3	0.97	0.72
	B2	96.5	119	113	5	1.05	0.81
	B3	96.5	119	114	4	1.04	0.81
C	C1	90	106	104	1	1.01	0.85
	C2	114	113	115	2	0.98	1.01
	C3	114	116	117	1	0.99	0.98
D	D1	96.4	113	117	4	0.96	0.86
	D2	116	118	120	1	0.99	0.98
	D3	116	124	123	1	1.01	0.93

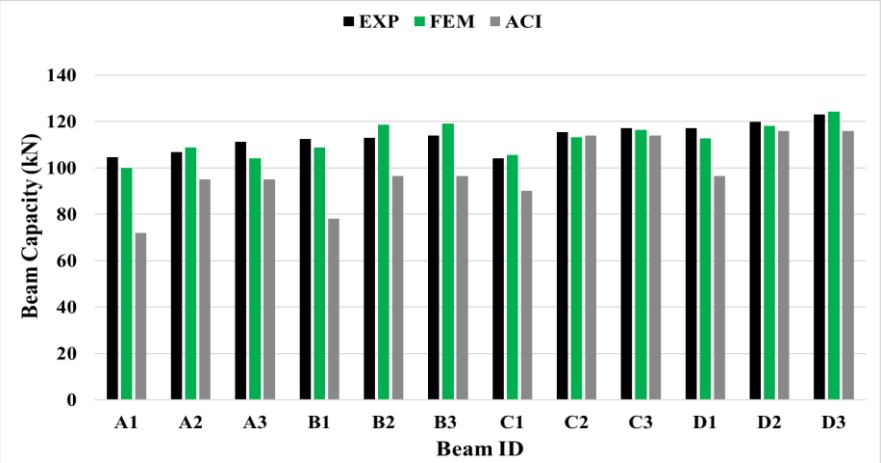

Fig. 34 ACI analytical, FEM and experimental Ultimate loads Values in all beams

correspondingly when contrasted to the collaborated magnitude for specimen (A2). Moreover, the vertical displacement at utmost load (δ1u) for specimens (B3), (C3), and (D3) was 63 percent, 62 percent, and 58 percent, correspondingly, when compared to the comparable magnitude for specimen (A3).

5.5 ACI Equation, FEM and experimental ultimate loads values

The FEM ultimate load in the complete tested beams is contrasted to analytical predictions given in the ACI 318-19 (Neale *et al.* 2005) in Fig. 34 and Table 6. The proportion of ACI and FEM ultimate loads varied between 72 and 101 percent. Due to the criteria of safety as prescribed by the ACI to assure conservative design, FEM and the experimental ultimate loads have higher values compared to ACI analytical values.

6. Conclusions

Nonlinear FE models were created and verified in this research to anticipate the behavior of RC beams reinforced by Nitnol intelligent rods utilizing the internal injection technique, and the following findings were drawn:

1. Finite Element analyses made by commercial ABAQUS can anticipate the behaviour of RC beams reinforced with Nitinol intelligent rods.
2. The use of Nitinol intelligent rods and internal injection method reduced the cracks formed in the concrete beam and increased the strength of the beam as well as enhancing the overall restoring behavior.
3. Finite Element model performance is equivalent to the experimental investigation utilized as a reference. The variances in terms of ultimate load capacity did not surpass 5%, when compared to experimental data.
4. Mesh convergence investigation demonstrated that a mesh size of 25 mm may accurately anticipate findings in an acceptable amount of time.
5. All of the above show that the ABAQUS numerical simulation software is competent, but the subject of how to acquire more precise results requires further research.

Based on the previous experimental &FEM results, the following points are recommended for further studies.

- In the future, there is hope to reach a fully automated system to perform high efficient self-repair by the internal injection in combination with smart bars.
- Reducing the injection materials healing time to be more effective in a short time to repair most of aftermath cracks.
- Internal hollow cores locations should be designed perfectly to give more efficiency in internal injection methods.
- SMA Smart bars locations in critical concrete section with proper design criteria have to be well studied to do high self-repair efficiency.

Acknowledgments

Thank you, Allah for assisting me in bringing this effort to light. I am grateful to Prof. Dr. Adil Kahwash Al-Tamimi, Civil Eng. Dept. College of Engineering Department, American University of Sharjah; UAE, and the laboratory crew for the helping, advising, and permitting to execute all experimental studies in the AUS laboratory with huge support process flow up to achieve the goal. I am grateful to Prof. Dr. Ali Elkhatib and Prof. Dr. Mohammed Mahmoud who supported the research proposal, deserve special thanks.

References

Abdulridha, A., Palermo, D., Foo, S. and Vecchio, F.J. (2013), "Behavior and modeling of superelastic shape memory alloy reinforced concrete beams", *Eng. Struct.*, **49**, 893-904. https://doi.org/10.1016/j.engstruct.2012.12.041

ACI Committee (2008), "Building code requirements for structural concrete (ACI 318-08) and commentary", American Concrete Institute.

Bykiv, N., Yasniy, P., Lapusta, Y. and Iasnii, V. (2022), "Finite element analysis of reinforced-concrete beam with shape memory alloy under the bending", *Proc. Struct. Integr.*, **36**, 386-393. https://doi.org/10.1016/j.prostr.2022.01.05

Daghia, F., Giammarruto, A. and Pascale, G. (2011), "Combined use of FBG sensors and SMA actuators for concrete beams repair", *Struct. Control Health Monitor.*, **18**(8), 908-921. https://doi.org/10.1002/stc.410

Elamary, A.S., Sharaky, I.A. and Alqurashi, M. (2021), "Flexural behaviour of hollow concrete beams under three points loading: Experimental and numerical study", *Structures*, **32**, 1543-1552). https://doi.org/10.1016/j.istruc.2021.03.094

Halahla, A.M., Tahnat, Y.B.A., Almasri, A.H. and Voyiadjis, G.Z. (2019), "The effect of shape memory alloys on the ductility of exterior reinforced concrete beam-column joints using the damage plasticity model", *Eng. Struct.*, **200**, 109676. https://doi.org/10.1016/j.engstruct.2019.109676

Hassan, H.S., Elkhatib, A.A., Ahmed, M.M. and Al-Tamimi, A.K. (2022), "Behaviour of self-repaired reinforced concrete beams made using smart materials under static cyclic loads (shear study)", *Structures*, **35**, 406-420. https://doi.org/10.1016/j.istruc.2021.11.024

Ji, S.W., Yeon, Y.M. and Hong, K.N. (2022), "Shear performance of RC beams reinforced with Fe-based shape memory alloy stirrups", *Materials*, **15**(5), 1703. https://doi.org/10.3390/ma15051703

Khalil, A., Elkafrawy, M., Abuzaid, W., Hawileh, R. and AlHamaydeh, M. (2022), "Flexural performance of RC beams strengthened with pre-stressed iron-based shape memory alloy (Fe-SMA) bars: numerical study", *Buildings*, **12**(12), 2228. https://doi.org/10.3390/buildings12122228

Khaloo, A.R., Eshghi, I. and Piran, A.P. (2010), "Study of behavior of reinforced concrete beams with smart rebars using finite element modeling", *Int. J. Civil Eng.*, **8**(3).

Kyaure, M. and Abed, F. (2021), "Finite element parametric analysis of RC columns strengthened with FRCM", *Compos. Struct.*, **275**, 114498. https://doi.org/10.1016/j.compstruct.2021.114498

Malagisi, S., Marfia, S., Sacco, E. and Toti, J. (2014), "Modeling of smart concrete beams with shape memory alloy actuators", *Eng. Struct.*, **75**, 63-72. https://doi.org/10.1016/j.engstruct.2014.05.035

Mazzoni, S., McKenna, F., Scott, M.H. and Fenves, G.L. (2006), "OpenSees command language manual", *Pacific Earthq. Eng. Res. (PEER) Center*, **264**(1),

Mohammadgholipour, A. and Billah, A.M. (2023), "Mechanical properties and constitutive models of shape memory alloy for structural engineering: A review", *J. Intell. Mater. Syst. Struct.*, **34**(20), 2335-2359. https://doi.org/10.1177/1045389X231185458

Neale, K.W., Ebead, U.A., Abdel Baky, H., Elsayed, W. and Godat, A. (2005), "Modelling of debonding phenomena in FRP-strengthened concrete beams and slabs", *Proceedings of the International Symposium on Bond Behaviour of FRP in Structures (BBFS 2005)*.

Obaidat, Y. (2011), *Structural Retrofitting of Concrete Beams Using FRP-Debonding Issues*, No. TVSM-1023, Lund University, Sweden.

Pawtucket, K. & S.I. (2014), *ABAQUS standard user's manual. Version 6.11*, *vol. IV*, U.S.A.

Ruiz-Pinilla, J.G., Montoya-Coronado, L.A., Ribas, C. and Cladera, A. (2020), "Finite element modeling of RC beams externally strengthened with iron-based shape memory alloy (Fe-SMA) strips, including analytical stress-strain curves for Fe-SMA", *Eng. Struct.*, **223**, 111152. https://doi.org/10.1016/j.engstruct.2020.111152

Supaviriyakit, T., Pornpongsaroj, P. and Pimanmas, A. (2004), "Finite element analysis of FRP-strengthened RC beams", *Songklanakarin J. Sci. Technol*, **26**(4), 497-507.

Wang, B. and Zhu, S. (2018), "Seismic behavior of self-centering reinforced concrete wall enabled by superelastic shape memory alloy bars", *Bull. Earthq. Eng.*, **16**(1), 479-502. https://doi.org/10.1007/s10518-017-0213-8

Yeon, Y.M., Lee, W. and Hong, K.N. (2022), "Finite element analysis of reinforced concrete beams prestressed by Fe-based shape memory alloy bars", *Appl. Sci.*, **12**(7), 3255. https://doi.org/10.3390/app12073255

List of Abbreviations

FEA	Finite Element Analysis
RC	Reinforced Concrete
SMA	Shape Memory Alloy;
SME	The shape memory effect
SE	Super Elastic effect
Nitnol	NiTi Alloy Nonlinear.
SC	self-centering
Fe-SMA	iron-based shape memory alloy
H.T.S	High Tensile Steel
FEM	Finite Element Modelling
Ast	Area of H.T.S stirrup
An	Area of Nitinol Rods
CMC	Cracking model for concrete
CSCM	Concrete smeared cracking model
CDPM	Concrete damaged plasticity model
f'_c	Concrete Compressive strength
E_c	Modulus of elasticity
v	Poisson's ratio
f'_{ct}	The Concrete tensile strength
ρw	Shear reinforcement ratios
Asw	Total area of stirrups legs crossing the crack/spacing (mm2)
S	stirrup spacing
Bw	beam width.
Δ	deflection at beam mid of span
P	Applied load